2025 IEEE/RSJ International Conference on Intelligent Robots and Systems (IROS 2025)
October 19-25, 2025. Hangzhou, China

2025 IEEE/RSJ International Conference on Intelligent Robots and Systems (IROS) | 979-8-3315-4393-8/25/$31.00 ©2025 IEEE | DOI: 10.1109/IROS60139.2025.11246477

Steering Elongate Multi-legged Robots by Modulating Body Undulation Waves

Esteban Flores*,1, Baxi Chong*,2, Daniel Soto[1], Daniel I. Goldman[2]

Abstract— **Centipedes exhibit great maneuverability in diverse environments due to their many legs and body-driven control. By leveraging similar morphologies and control strategies, their robotic counterparts also demonstrate effective terrestrial locomotion. However, the success of these multi-legged robots is largely limited to forward locomotion; steering is substantially less studied, in part because of the difficulty in coordinating a high degree-of-freedom robot to follow predictable, planar trajectories. To resolve these challenges, we take inspiration from control schemes based on geometric mechanics(GM) in elongate systems' locomotion through highly damped environments. We model the elongate, multi-legged system as a "terrestrial swimmer" in highly frictional environments and implement steering schemes derived from low-order templates. We identify an effective turning strategy by superimposing two traveling waves of lateral body undulation and further explore variations of the "turning wave" to enable a spectrum of arc-following steering primitives. We test our hypothesized modulation scheme on a robophysical model and validate steering trajectories against theoretically predicted displacements producing steering radii between 0 and 0.6 body length. We then apply our control framework to Ground Control Robotics' elongate multi-legged robot, Major Tom, using these motion primitives to autonomously navigate around obstacles and corners on indoor and outdoor terrain. Our work creates a systematic framework for controlling these highly mobile devices in the plane using a low-order model based on sequences of body shape changes.**

Fig. 1. Developing turning strategies that can enable steering and curved paths in multilegged robots. Ground Control Robotics Inc. robot, Major Tom, autonomously steering around a tree by detection of the obstacle with a force sensitive antenna and using amplitude modulation of the turning wave scheme described in this paper.

I. Introduction

Multi-legged robots can traverse rugged landscapes without the need for extensive sensing due to their many legs, making them appealing for various sectors such as search-and-rescue[1], agriculture[2], and terrestrial exploration. Unlike few-legged systems where effective locomotion relies on the precise control of each leg, a many-legged system can continue to successfully locomote after individual leg failure or missed contacts because of their morphological redundancy [3], [4]. Despite this robustness, whole-body coordination in multi-legged robots (Fig. 1) (e.g., body bending, leg stepping, and leg rotation) presents a high degree-of-freedom (DoF) problem that increases in complexity with the number of legs. To reduce the dimensionality of this control problem, schemes based on geometric phase produce effective locomotion by treating elongate locomotors as terrestrial swimmers in highly damped environments[5]. Using this approach, elongate robot control is simplified to the propagation of a traveling wave down the body with a coupled leg wave similar to biological systems, achieving robust, agile locomotion using a low-dimensional template that is not limited by number of segments [6][4]. However, the success of controlling elongate, multi-legged robots using this scheme has been limited to generating forward motion. The significant research gap in producing more complex trajectories for myriapod robots limits their applicability. Having the ability to steer along arcs is essential for navigation in cluttered environments and path planning.

Traditional approaches to steering legged systems take inspiration from the success of wheeled systems that involve an imbalance of angular velocities to create arcs (Fig. 2A.2). The differential drive approach is widely adapted for few-legged robots such as quadrupeds or bipeds. Previous work has shown that careful foot placement planning with rigid bodies can enable quadrupedal turning motions that include considerations for speed, stability, and translation direction

*These authors contributed equally to this work.
[1]E. Flores and D. Soto are with Ground Control Robotics Inc. Email: eflores36@gatech.edu, *gcrobotics314@gmail.com*.
[2]B. Chong and D. I. Goldman are with the School of Physics, Georgia Institute of Technology, Atlanta, GA, 30332 USA. Email: *bchong9@gatech.edu,daniel.goldman@physics.gatech.edu*
Corresponding author: Daniel I. Goldman

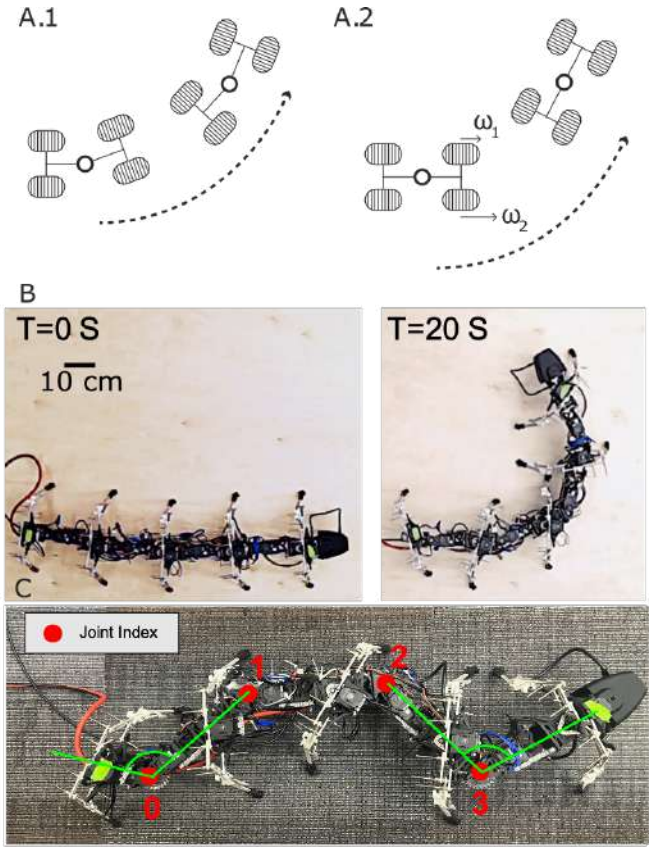

Fig. 2. Comparing wheeled vehicle steering strategies to body driven turning in multilegged robots (A.1) Ackerman steering strategy in a 4 wheeled vehicle utilizing changes to wheel orientation. (A.2) Differential drive steering strategy utilizing rotational velocity imbalance to induce turns on a wheeled vehicle. (B) Centipede robot steering strategy powered by body shape changes similar to Ackerman steering. (C) Horizontal body undulation joint index and angle definition

[7][8].

However, the differential drive approach is poorly suited to elongate multi-legged, robots partially because of their relatively simple legs (e.g., mechanical constraints on leg actuation) and their redundant ground reaction force (the differential torque from each leg pair may cancel with each other). Instead, strategies generated by body deformation, similar to Ackerman steering in wheeled systems, (Fig. 2A.1) are more readily applicable to elongate systems. As a result, previous steering schemes for myriapod robots leverage mechanically induced body asymmetry dependent on robot design[9], low-level control of foot contact and body angles[10], or asymmetries in phase or amplitude of central pattern generator systems. [11].

We present a template for steering gaits in elongate, multilegged systems using sequences of body shape changes which are readily generalizable to multiple platforms without extensive tuning or low-level joint planning. We use tools from geometric mechanics (GM) to develop gait sequences and simplify seemingly complex locomotive behavior [12], [13], [14], [15], [16], [17], [6]. Building upon success in steering elongate limbless robots [18], [19], we posit similar body-driven turning strategies can be applied to elongate, multi-legged devices because they share a common locomotion framework in environments where damping forces dominate inertial forces [5].

We propose a control strategy that is capable of generating a wide variety of circular arcs by introducing a second traveling wave to the horizontal body undulation (i.e., internal joint angles Fig. 2.C) while keeping the same coupled leg wave used in forward locomotion [5]. We implemented this strategy on a robophysical model and on a simulation and varied the parameters of the second wave. Notably, the two approaches show close agreement, demonstrating the predictive capability of the two-wave template in designing gaits for undulatory, multi-legged locomotors. In collaboration with Ground Control Robotics Inc, we implemented the steering template on a myriapod robot, Major Tom [20], for autonomous navigation in indoor and outdoor terrain using the onboard force-sensitive antenna [21] (Fig. 1). Our results significantly enrich the library of locomotion strategies for elongate multi-legged robots and provide effective tools to navigate around obstacles, paving the way towards all-terrain, highly-capable, elongate multi-legged robots.

II. Geometric Mechanics

A. Two basis function turning

To prescribe horizontal body undulations, we first create a low-dimensional space for multi-legged locomotion. As documented in prior work [4], [5], we assume that the lateral body undulation wave can be prescribed by:

$$\begin{aligned} \alpha(i,t) &= w_1(t)S_1(i) + w_2(t)S_2(i) \\ S_1(i) &= \sin\left(2\pi k_0 \frac{i}{N}\right) \\ S_2(i) &= \cos\left(2\pi k_0 \frac{i}{N}\right) \end{aligned} \tag{1}$$

where $\alpha(i,t)$ denotes the yaw angle of i-th joint at time t (Fig. 2C); $S_1(i)$ and $S_2(i)$ are shape basis functions with spatial frequency, or number of waves on the body, k_0; N is the number of leg pairs; $w_1(t)$ and $w_2(t)$ are the time series of weights for the corresponding shape basis functions. Here, we define the shape variable as $\boldsymbol{w}(t) = [w_1(t), w_2(t)]$, which then uniquely characterizes the body movement. As discussed in prior work [4], [5], the contact pattern of legs and the leg shoulder angles can also be prescribed by the shape variable $\boldsymbol{w}$ (detailed prescription equations can be found in [4]). In Fig.3.A, we illustrated the shape space for a 10-legged robot offset turn which allows for easy comparison of a gait cycle to the two-wave template (Fig. 4).

Perturbation in the shape variable can result in net displacement. The net translation in the plane, SE(2), can be characterized by Δx, Δy, $\Delta\theta$ in forward, lateral, and rotational directions, respectively. To better characterize turning/steering in SE(2), we use the following notation to describe the net translation in the plane: r, $\Delta\theta$, and γ, which characterize the steering curvature, rotational translation, and changes in the heading directions, respectively (Fig. 5). Notably, for small perturbations in the shape variables

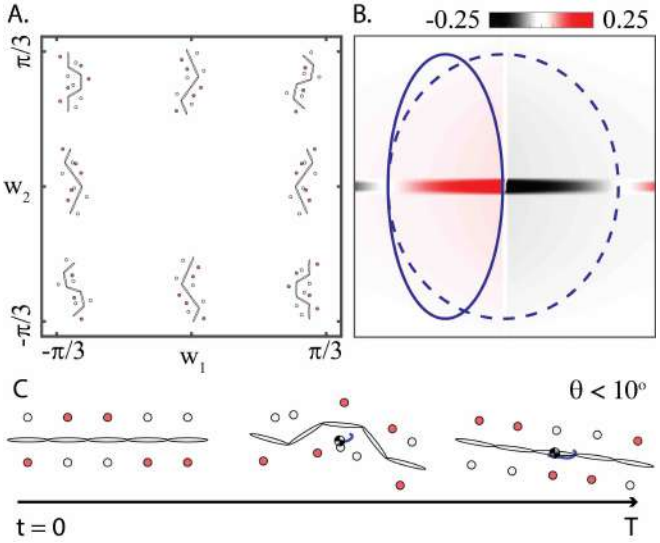

Fig. 3. Geometric mechanics for turning in a Euclidean shape space. (A) The shape space for a multi-legged robot represented by a two-wave template. Robot body postures over the shape space are presented. (B) The rotational height functions using the two-wave template. Turning can be modulated by offsetting a gait path from the center (enclosing non-zero surface integral over the height function). Paths in shape space prescribe a series of robot shapes and coupled contact patterns that define a gait. (C) An example simulation of the gait leading to net heading angle change less then 10°

(thus, small displacements), we have: $r\Delta\theta = |[\Delta x, \Delta y]|$, and $\tan(\gamma) = \Delta y/\Delta x$.

We define the body velocity, $\boldsymbol{\xi} = [\xi_x, \xi_y, \xi_\theta]$, as the overall locomotor velocity in the forward, lateral, and rotational directions [22]. Specifically, we have: $\boldsymbol{\xi} = \lim_{t\to 0} \frac{[\Delta x,\ \Delta y,\ \Delta\theta]}{dt}$. We can then numerically calculate the body velocity from shape variables ($\boldsymbol{w}$) and the shape velocity ($\dot{\boldsymbol{w}}$) via net ground reaction force (GRF) analysis. Here, we model the ground reaction force by rate independent Coulomb friction. From geometry, the GRF at each foot can be uniquely expressed as a function of shape variable ($\boldsymbol{w}$), shape velocity ($\dot{\boldsymbol{w}}$), and body velocity ($\boldsymbol{\xi}$). Assuming quasi-static motion, we consider the total net force applied to the system is zero at any instant in time:

$$\boldsymbol{F} = \sum_{i\in I_{\boldsymbol{w}}} \left[\boldsymbol{F}^i_{\parallel}(\boldsymbol{\xi}, \boldsymbol{w}, \dot{\boldsymbol{w}}) + \boldsymbol{F}^i_{\perp}(\boldsymbol{\xi}, \boldsymbol{w}, \dot{\boldsymbol{w}})\right] = 0, \quad (2)$$

where $I_{\boldsymbol{w}}$ is the collection of all stance-phase legs, determined by the shape variable $\boldsymbol{w}$ [4]. At a given body shape $\boldsymbol{w}$, Eq.(2) connects the shape velocity $\dot{\boldsymbol{w}}$ to the body velocity $\boldsymbol{\xi}$. Therefore, by the implicit function theorem and the linearization process, we can numerically derive the fundamental equation of motion:

$$\boldsymbol{\xi} \approx \boldsymbol{A}(\boldsymbol{w})\dot{\boldsymbol{w}} = \begin{bmatrix} \boldsymbol{A}^x(\boldsymbol{w}) \\ \boldsymbol{A}^y(\boldsymbol{w}) \\ \boldsymbol{A}^\theta(\boldsymbol{w}) \end{bmatrix} \dot{\boldsymbol{w}}, \quad (3)$$

where $\boldsymbol{A}$ is the local connection matrix, $\boldsymbol{A}^x, \boldsymbol{A}^y, \boldsymbol{A}^\theta$ are the three rows of the local connections, respectively. Each row of the local connection matrix can be regarded as a vector field over the shape space, called the connection vector field. In this way, the body velocities in the forward, lateral, and rotational directions are computed as the dot product of connection vector fields and the shape velocity $\dot{\boldsymbol{w}}$.

Consider a gait as a periodic pattern of self-deformation: $\{\partial\phi\ : [w_1(t), w_2(t)], t \in (0, T]\}$, where T is the temporal period. The displacement along the gait path $\partial\phi$ over a cycle can be approximated to the first order by:

$$\begin{pmatrix} \Delta x \\ \Delta y \\ \Delta\theta \end{pmatrix} = \int_{\partial\phi} \begin{bmatrix} \boldsymbol{A}^x(\boldsymbol{w}) \\ \boldsymbol{A}^y(\boldsymbol{w}) \\ \boldsymbol{A}^\theta(\boldsymbol{w}) \end{bmatrix} \mathrm{d}\boldsymbol{w}. \quad (4)$$

To analyze turning gaits, we have $\Delta\theta = \int_{\partial\phi} \boldsymbol{A}^x(\boldsymbol{w})\mathrm{d}\boldsymbol{w}$. According to Stokes' Theorem, the line integral along a closed curve $\partial\phi$ is equal to the surface integral of the curl of $\boldsymbol{A}^\theta(\boldsymbol{w})$ over the surface enclosed by $\partial\phi$:

$$\Delta\theta = \int_{\partial\phi} \boldsymbol{A}^\theta(\boldsymbol{w})\mathrm{d}\boldsymbol{w} = \iint_{\phi} \nabla \times \boldsymbol{A}^\theta(\boldsymbol{w})\mathrm{d}w_1\mathrm{d}w_2, \quad (5)$$

where ϕ denotes the surface enclosed by $\partial\phi$. The curl of the connection vector field, $\nabla \times \boldsymbol{A}^\theta(\boldsymbol{w})$, is referred to as the height function [23]. With the above derivation, the gait design problem is simplified to drawing a closed path in the shape space. Net displacement over a period can be approximated by the integral of the surface enclosed by the gait path. Hence, we are able to visually identify the optimal gait leading to the largest turning by finding the path with the maximum surface integral.

We illustrate the height function and an example gait path in Fig.3B. From the structures of height functions, we notice that (1) the positive and negative volumes are distributed symmetrically about the y-axis ($w_1 = 0$), and (2) turning can be induced if we introduce an offset to the center of the gait path (solid path in Fig.3B). As documented in [6], adding an offset to the gait path in the shape space is an effective turning strategy for limbless locomotors such as nematode worms and sidewinders. However, we also note that the magnitude of the rotational height function is small, leading to a relatively ineffective turning strategy. To verify our observation, we test the center-shifted path (the solid path in Fig. 3B) in simulation, and we note that the net turning over a cycle is less than 10°. We posit that leveraging previous work in limbless locomotion could enable more effective steering schemes, specifically through the addition of basis functions.

B. Three basis function turning

We hypothesize that effective turning schemes in nematodes [18], [19] may be applicable for multi-legged locomotors because of the similarity in their body driven locomotion through low-inertial regimes. Specifically, we introduce the third basis function:

$$\alpha(i,t) = w_1(t)S_1(i) + w_2(t)S_2(i) + w_3(t)S_3 i$$
$$S_3(i) = \cos(2\pi k_1 \frac{i - N/2}{N}) \quad (6)$$

where k_1 is the spatial frequency of the third wave. For simplicity, we first consider $k_1 = 0$ in this section. The third basis function introduces a 3-dimensional shape space, which can present a substantial challenge for directly applying geometric mechanics [24], [25]. To simplify our analysis, we chose a fixed prescription on the trajectory in w_1-w_2 space:

$$w_1 = \pi/6 \cos(\phi) \tag{7}$$
$$w_2 = \pi/6 \sin(\phi), \tag{8}$$

where ϕ denotes the phase. Thus, we construct a new

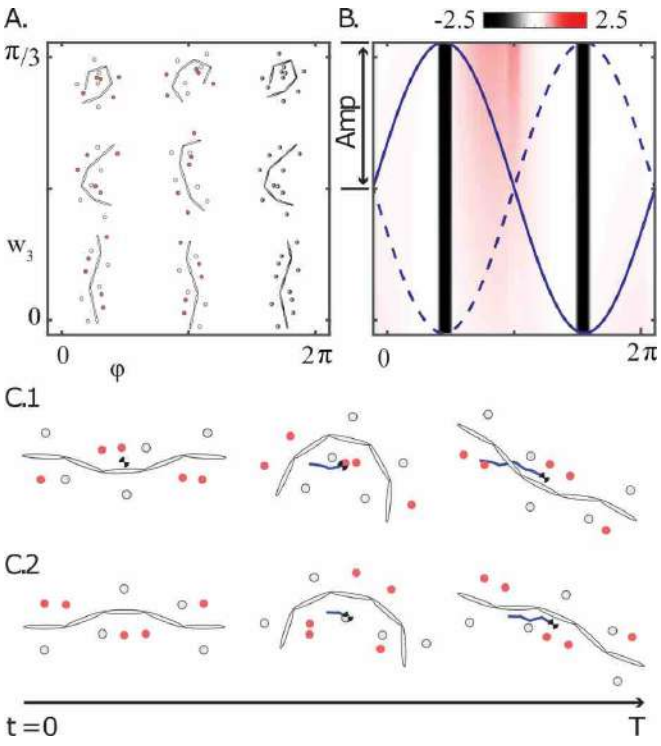

Fig. 4. Geometric mechanics in a cylindrical shape space (A) The shape space for a multi-legged robot represented by a three-wave template. Y-axis denotes the amplitude of the third wave. The x-axis denotes the phase in the first-two waves. (B) The corresponding rotational height functions. We identified two effective steering gaits illustrated in solid and dash curves. The steering gaits can be prescribed by a sinusoidal function with a constant offset. (C) simulation of the two steering gaits.

shape space $\boldsymbol{C} = [\phi,\ w_3]$. Notably, $\boldsymbol{C}$ has a cylindrical structure [26] because ϕ is periodic (i.e., $\phi = 0$ is equivalent to $\phi = 2\pi$). We illustrate the new shape space in Fig. 4. Following similar steps as described in Sec. II.A, we obtain the height function in the new shape space (Fig. 4B). Notably, the new rotational height function is an order of magnitude greater than two basis turning and the gait area (e.g., the solid and dashed line in Fig. 4B) can be calculated as the area underneath the curve, despite the curve not forming a closed surface [27], [28].

We thus identify two effective turning gaits, represented by the solid and dashed curves in Fig. 4B:

$$w_3 = A_3 \sin(\phi) \text{ or,} \tag{9}$$
$$w_3 = A_3 \sin(\phi + \pi) \tag{10}$$

We verify the effectiveness using numerical simulation in Fig. 4C. Both gaits can lead to net rotation over 20° per cycle, and we choose (Eq. 9) for further analysis. Specifically, we consider a modulation on the amplitude (A_3). We hypothesize that the modulation on this amplitude can enable a control over the net rotation $\Delta\theta$ and turning curvature r. To test our hypothesis, we performed the numerical simulation to estimate the net rotation $\Delta\theta$ and turning curvature r as a function of A_3 (numerical simulation details can be found in [18], [19], [6]). As a result, we notice an almost linear relationship (Fig. 6.A, red curves) between the amplitude (A_3) and the net turning ($\Delta\theta$) or steering curvature ($1/r$).

III. Experimental Setup

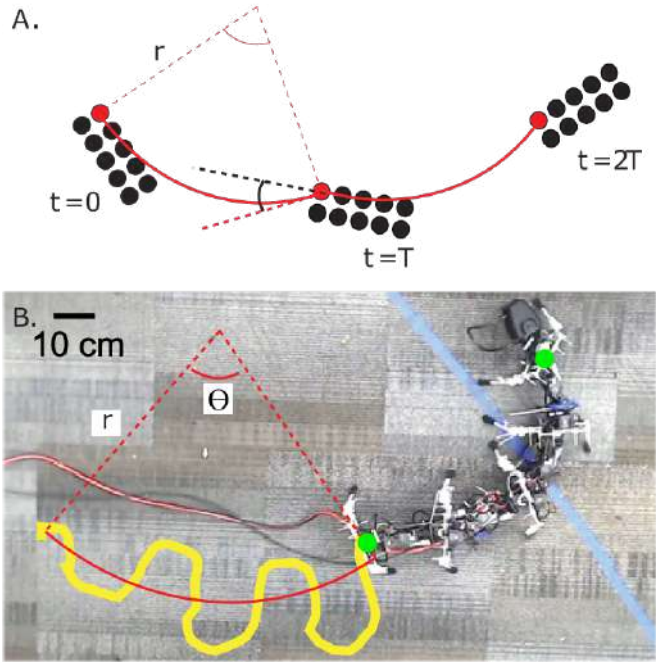

Fig. 5. Testing turning behaviors in a robophysical model. (A) An illustration of a 10 -legged robot steering over two cycles. The red curve denotes the trajectory of the rear, left leg. Steering parameters are labeled: steering radius, r, heading angle change, θ, and orientation change angle from the tangent, γ. (B) Markers on robophysical model, marked in green, are placed on the first and last module of the robot. The yellow curve denotes the marker trajectory over 3 cycles. The red curves are the fitted circle to estimate steering parameters. For visual clarity, only the rear marker trajectory and curve fit are shown. The pose of the robot is defined as the vector at any time from the tail marker to the head marker.

To test the possible turning behavior, we built a five-segment, 10-legged robophysical model with the ability to control horizontal and vertical body joint angles, leg rotation angles, and leg stepping contacts. Additionally, it has an on-board computer (Raspberry Pi 4), head module with a depth camera (Intel© RealSense™), that was not used for this study. Horizontal and vertical body undulation are controlled via Dynamixel 2XL430 servos while leg rotation and stepping motions use Dynamixel XL430 servos. Mechanical gears, with a 2:1 ratio, increase the torque of the body servos while rigid linkages control the stepping motion. There are ball

casters on the tips of the limbs to allow for free rotation on the carpet surface during contact and to limit sinkage.

We define steering paths as circular arcs of fixed radius, r, where the heading angle change, θ, describes the amount of the arc that is traversed, and γ describes the rotation of the robot relative to the tangent of the arc. A planar steering path can be fully defined by these three parameters for each robot cycle ($t = T$) as shown in Fig. 5A.

We measured steering trajectories on the robot by tracking markers via an overhead camera (Fig. 5B). To reduce variability from body undulations, the average position of two markers and the vector from tail to head defines the pose of the robot body. A circle is fit to the trajectory of the robot after 3 cycles to obtain r while θ is obtained by taking the angle between the initial and final pose of the robot. Similarly, γ is calculated as the angle between the tangent of the fitted circle and the pose of the robot. Both θ and γ are divided by the number of cycles (in our case, 3) to obtain the average angular displacement per cycle for each trial.

IV. Experimental Results

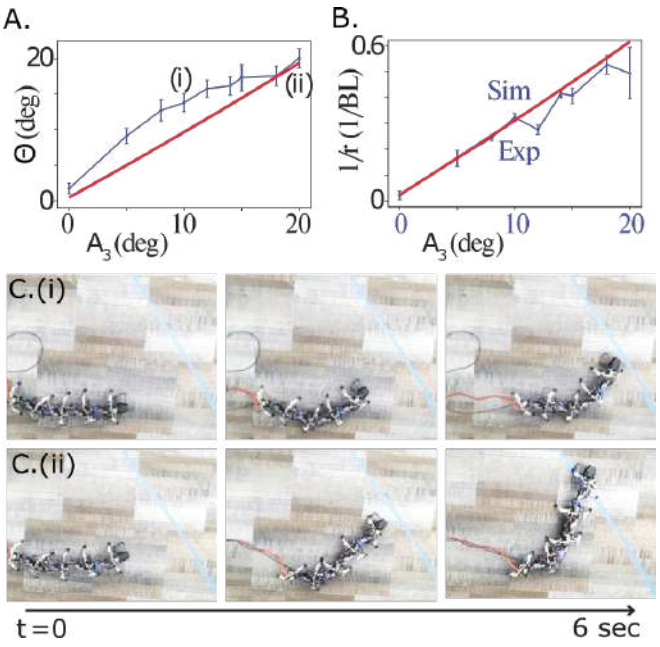

Fig. 6. Experimental and simulation results of (A) heading angle change change per cycle and (B) curvature per cycle for a range of amplitudes (A_3). The points are the average of 5 trials and error bars are plus, minus one standard deviation. (C) By modulating the amplitude of the third wave, different steering paths can be induced on a multi-legged robot.

A. Amplitude Modulation

We varied the amplitude of A_3 and plot the mean and standard deviation in Figure 6. The heading angle change and curvature ($\frac{1}{r}$) at amplitudes $A \in [0 - 20°]$ demonstrate a proportionally increasing relationship with A_3 (Fig. 6). The resulting average heading angle change shows an increasing trend that appears to be linearly related to A_3 until it begins to saturate after $10°$ where the slope decreases (Fig. 6A). Additionally, due to self collisions at large body joint angles, amplitudes greater than $20°$ are not possible, yielding a maximum heading angle change of 20 ± 1.4 degrees per cycle. Similarly, the curvature of the steering arcs generally increases with amplitude (Fig.6B), demonstrating that smaller steering radii are achievable with an inversely proportional relationship to amplitude. We observed the greatest heading angle change with $A_3 = 20$ resulting in the robot sweeping $60°$ over the course of 3 cycles. Interestingly, numerical simulations (Fig.6) for curvature based on GM closely match the linear relationship and bounds for the curvature while the predictions for heading change underestimate a significant portion of the data. This is potentially due to the discrepancy between the actual ground reaction force between the robot and the carpet and to the assumed Coulomb friction model.

The arc length of the robot path is obtained by multiplying θ by the steering radius, r, and it remains relatively constant until $A_3 = 10°$, where the total path traveled decays as total translation decreases for larger angle rotations with small turning radii. This indicates that for small amplitude turns the robot can maintain its net displacement equivalent to purely forward motion ($0°$) while its net displacement slowly decays on larger amplitude turns. The rotation angle γ remained constant and close to zero ($< 4°$) throughout the cycle for each amplitude. While only counterclockwise (CCW) steering data was tracked and reported, clockwise (CW) steering is achieved by negating the shape bases and steering backward requires changing the sign of the first temporal basis function w_1.

B. Spatial Basis Manipulation

Our results show that amplitude modulation of a second traveling wave is an effective and simple control for generating steering paths in multi-legged systems. However, the third shape basis function, S_3 remained constant at [1,1,1,1], denoted as S_3^1, which corresponds to $k_1 = 0$. To investigate the effects of modulating this basis, we conducted trials at two additional static values of $S_3^2 = [1, .5, .5, 1]$ and $S_3^2 = [1, 0, 0, 1]$, which approximates a spatial frequency of $k_1 = .2$ and $k_1 = .4$ respectively (Fig. 7). The comparison of the three fixed basis functions demonstrates that manipulation of the third shape basis allows for a wider range of steering trajectories suggesting a second form of control for motion in $SE(2)$. This data suggests a future avenue for modeling and experiments with a varying S_3 to increase the total steering space in $SE(2)$ possible for multi-legged robot locomotion.

V. From Robophysics to Robotics

Using the empirically derived steering strategies as basic motion primitives, smooth planar motion can be achieved by sequencing these arcs with forward motion to achieve efficient navigation and obstacle avoidance (Fig. 8A). The demonstration of the robophysical model turning around a corner in open-loop control, a case where both steering CCW and steering CW are required, shows how left turn, right turn, and forward gait patterns can be sequenced together. Achieving this relatively complex path of sequencing arcs only involves changing the value and sign of A_3 from negative

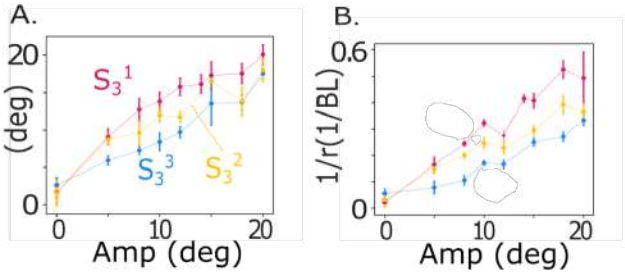

Fig. 7. Experimental results for robot turning (A) heading and (B) curvature for three different basis functions S_3^2, S_3^2 and S_3^3

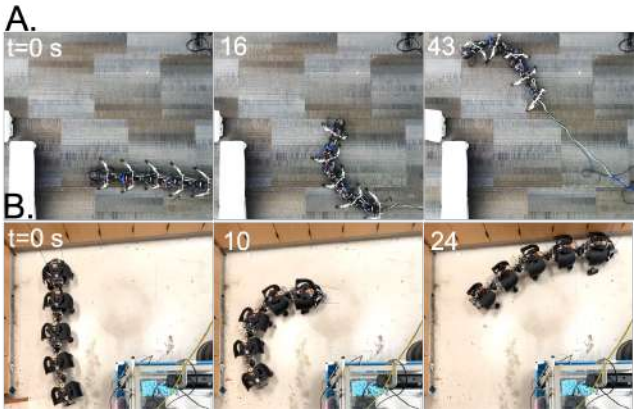

Fig. 8. Testing turning behaviors in the presence of obstacles (A) Robophysical model performing an S-shaped trajectory around a wall only using amplitude modulation; Varying A_3 from positive to negative between each gait cycle allows for smooth transitions between right and left turning (B) Ground Control Robotics Inc. Major Tom performing autonomous wall following algorithm using amplitude modulation steering; Sensing of the wall is done with two force sensitive antenna detecting objects positioned ahead or laterally

to positive in between cycles while modulating the absolute value dictates the radius of the turn. The path in Fig. 8 was generated by commanding a positive, zero, and negative A_3 to sequence right, forward, and left motions respectively. This demonstrates the power of the dimensionally reduced template for control of high-degree-of-freedom robots and steer in cluttered environments where obstacles must be avoided instead of traversed.

Extending this template to autonomous navigation, a test was conducted using Ground Control Robotics Inc.'s (5-link, 1.8 m) Major Tom robot (Fig. 8). Using feedback from on-board force-sensing antenna, the robot successfully detected the wall and navigated the corner autonomously using only amplitude modulation of a third basis function. Furthermore, preliminary autonomous tests are conducted outside in highly cluttered, rugose environments allowing for navigation in scenarios that would otherwise result in collisions.(Fig. 1). The extension of the steering template to Ground Control Robotics' Major Tom, approximately five times heavier (10 kg) and 1.5 times longer than the robophysical model, proves the strength of the dimensionality reduction methods used to control high DOF, undulatory systems while the effectiveness of the steering performance on a variety of terrains (carpet, linoleum, leaves, and dirt) validate the control assumptions of these terrestrial swimmers in low-inertia environments.

VI. Conclusion and Future Work

Through tools established for limbless locomotors, we present a novel turning scheme that extends previous research in coordinating limbless robots to multi-legged robots by the modulation of an additional traveling wave down the body of the robot which generates a wide variety of steering arcs. Using simulation and robophysical experiments, we found two key variables in controlling steering angles: A_3, the amplitude of the second wave, and S_3, the spatial basis function. While a sufficient range of possible amplitudes were swept, predicting and testing the relationship between spatial frequency modulation and turning performance remains a subject for future work. Additionally, investigating the validity of the Coulomb friction model in the GM framework as a source for the discrepancy between the predictions and experiments, steering efficacy on highly rugged terrain where foot contacts are regularly missed, and the role of leg dynamics may yield more effective steering schemes and further insights into controlling these systems. To enable higher amplitude turns on future robots, larger inter-segment spacing or the use of compliant materials may mitigate the effects of detrimental self collisions.

This scheme builds upon previous work done in shape-based control of multi-legged robots that has proven to be robust across rugged terrain[3]. By testing on a variety of terrains (carpet, hard floor, outdoors), we strengthened the locomotive assumptions in the model for moving in highly damped environments. Further, the predicted turning arcs serve as motion primitives that are important for a broad range of locomotion tasks, particularly those involving autonomous navigation in complex environments and obstacle avoidance. Because of the simple amplitude modulation scheme, implementation into closed-loop control involves manipulating only one variable for future real-time course correction. We successfully leveraged this fact for basic obstacle avoidance and wall-following algorithms and unlocked potential for work in full-trajectory planning for this class of robots. This ability to control planar trajectories serves as a substantial step forward in the mobile applications of multi-legged robot systems, particularly in motion planning and autonomous navigation.

Acknowledgments

We would like to thank Erik Teder and Juntao He for discussion and consultation. We would like to thank the Georgia Tech Institute for Robotics and Intelligent Machines for use of the College of Computing basement as a testing space. Additionally, we thank Ground Control Robotics Inc. for use of their robotic platform. The authors received funding from NSF-Simons Southeast Center for Mathematics and Biology (Simons Foundation SFARI 594594), Army Research Office grant W911NF-11-1-0514, a Dunn Family Professorship, Ground Control Robotics, and a STTR Phase I (2335553) NSF grant.

REFERENCES

[1] Kazuyuki Ito and Shota Kashiwada. Proposal of semiautonomous centipede-like robot for rubbles. *Artificial Life and Robotics*, 19(4):400–405, Dec 2014.

[2] S. M. Pedersen, S. Fountas, H. Have, and B. S. Blackmore. Agricultural robots–system analysis and economic feasibility. *Precision Agriculture*, 7(4):295–308, 09 2006. Copyright - Springer Science+Business Media, LLC 2006; Last updated - 2023-12-03.

[3] Baxi Chong, Juntao He, Daniel Soto, Tianyu Wang, Daniel Irvine, Grigoriy Blekherman, and Daniel I Goldman. Multilegged matter transport: A framework for locomotion on noisy landscapes. *Science*, 380(6644):509–515, 2023.

[4] Baxi Chong, Yasemin O Aydin, Jennifer M Rieser, Guillaume Sartoretti, Tianyu Wang, Julian Whitman, Abdul Kaba, Enes Aydin, Ciera McFarland, Kelimar Diaz Cruz, et al. A general locomotion control framework for multi-legged locomotors. *Bioinspiration & Biomimetics*, 17(4):046015, 2022.

[5] Baxi Chong, Juntao He, Shengkai Li, Eva Erickson, Kelimar Diaz, Tianyu Wang, Daniel Soto, and Daniel I Goldman. Self-propulsion via slipping: Frictional swimming in multilegged locomotors. *Proceedings of the National Academy of Sciences*, 120(11):e2213698120, 2023.

[6] Jennifer M Rieser, Baxi Chong, Chaohui Gong, Henry C Astley, Perrin E Schiebel, Kelimar Diaz, Christopher J Pierce, Hang Lu, Ross L Hatton, Howie Choset, et al. Geometric phase predicts locomotion performance in undulating living systems across scales. *Proceedings of the National Academy of Sciences*, 121(24):e2320517121, 2024.

[7] Zeungnam Bien, Myung-Geun Chun, and HS Son. An optimal turning gait for a quadruped walking robot. In *Proceedings IROS'91: IEEE/RSJ International Workshop on Intelligent Robots and Systems' 91*, pages 1511–1514. IEEE, 1991.

[8] DJ Cho, JH Kim, and Dae-Gab Gweon. Optimal turning gait of a quadruped walking robot. *Robotica*, 13(6):559–564, 1995.

[9] Shinya Aoi, Yuki Yabuuchi, Daiki Morozumi, Kota Okamoto, Mau Adachi, Kei Senda, and Kazuo Tsuchiya. Maneuverable and efficient locomotion of a myriapod robot with variable body-axis flexibility via instability and bifurcation. *Soft Robotics*, 10(5):1028–1040, 2023. PMID: 37231619.

[10] Yasemin Ozkan-Aydin and Daniel I Goldman. Self-reconfigurable multilegged robot swarms collectively accomplish challenging terradynamic tasks. *Science Robotics*, 6(56):eabf1628, 2021.

[11] Nopparuj Mingchinda, Vatsanai Jaiton, Benedict Leung, and Poramate Manoonpong. Leg-body coordination strategies for obstacle avoidance and narrow space navigation of multi-segmented, legged robots. *Frontiers in Neurorobotics*, 17:1214248, 2023.

[12] Robert W Batterman. Falling cats, parallel parking, and polarized light. *Studies in History and Philosophy of Science Part B: Studies in History and Philosophy of Modern Physics*, 34(4):527–557, 2003.

[13] Scott D Kelly and Richard M Murray. Geometric phases and robotic locomotion. *Journal of Robotic Systems*, 12(6):417–431, 1995.

[14] Jerrold E Marsden. Geometric foundations of motion and control. In *Motion, Control, and Geometry: Proceedings of a Symposium, Board on Mathematical Science, National Research Council Education, National Academies Press, Washington, DC*, 1997.

[15] Jim Ostrowski and Joel Burdick. The geometric mechanics of undulatory robotic locomotion. *The international journal of robotics research*, 17(7):683–701, 1998.

[16] Alfred Shapere and Frank Wilczek. Geometry of self-propulsion at low reynolds number. *Journal of Fluid Mechanics*, 198:557–585, 1989.

[17] Frank Wilczek and Alfred Shapere. *Geometric phases in physics*, volume 5. World Scientific, 1989.

[18] Tianyu Wang, Baxi Chong, Kelimar Diaz, Julian Whitman, Hang Lu, Matthew Travers, Daniel I Goldman, and Howie Choset. The omega turn: A biologically-inspired turning strategy for elongated limbless robots. In *2020 IEEE/RSJ International Conference on Intelligent Robots and Systems (IROS)*, pages 7766–7771. IEEE, 2020.

[19] Tianyu Wang, Baxi Chong, Yuelin Deng, Ruijie Fu, Howie Choset, and Daniel I Goldman. Generalized omega turn gait enables agile limbless robot turning in complex environments. In *2022 International Conference on Robotics and Automation (ICRA)*, pages 01–07. IEEE, 2022.

[20] Ground Control Robotics. Ground Control Robotics Website. `https://groundcontrolrobotics.com/`, 2025. Accessed: Mar. 3, 2025.

[21] Juntao He, Baxi Chong, Massimiliano Iaschi, Vincent R Nienhusser, Sehoon Ha, and Daniel I Goldman. Tactile sensing enables vertical obstacle negotiation for elongate many-legged robots. *arXiv preprint arXiv:2504.08615*, 2025.

[22] Richard M Murray, Zexiang Li, S Shankar Sastry, and S Shankara Sastry. *A mathematical introduction to robotic manipulation*. CRC press, 1994.

[23] Ross L Hatton and Howie Choset. Nonconservativity and noncommutativity in locomotion. *The European Physical Journal Special Topics*, 224(17-18):3141–3174, 2015.

[24] Baxi Chong, Yasemin Ozkan Aydin, Guillaume Sartoretti, Jennifer M Rieser, Chaohui Gong, Haosen Xing, Howie Choset, and Daniel I Goldman. A hierarchical geometric framework to design locomotive gaits for highly articulated robots. In *Robotics: science and systems*, 2019.

[25] Suresh Ramasamy and Ross L Hatton. Soap-bubble optimization of gaits. In *2016 IEEE 55th Conference on Decision and Control (CDC)*, pages 1056–1062. IEEE, 2016.

[26] Baxi Chong, Yasemin Ozkan Aydin, Chaohui Gong, Guillaume Sartoretti, Yunjin Wu, Jennifer M Rieser, Haosen Xing, Perrin E Schiebel, Jeffery W Rankin, Krijn B Michel, et al. Coordination of lateral body bending and leg movements for sprawled posture quadrupedal locomotion. *The International Journal of Robotics Research*, 40(4-5):747–763, 2021.

[27] Chaohui Gong, Zhongqiang Ren, Julian Whitman, Jaskaran Grover, Baxi Chong, and Howie Choset. Geometric motion planning for systems with toroidal and cylindrical shape spaces. In *Dynamic Systems and Control Conference*, volume 51913, page V003T32A013. American Society of Mechanical Engineers, 2018.

[28] Bo Lin, Baxi Chong, Yasemin Ozkan-Aydin, Enes Aydin, Howie Choset, Daniel I Goldman, and Greg Blekherman. Optimizing coordinate choice for locomotion systems with toroidal shape spaces. In *2020 IEEE/RSJ International Conference on Intelligent Robots and Systems (IROS)*, pages 7501–7506. IEEE, 2020.